Journal Name

ARTICLE TYPE

Cite this: DOI: 00.0000/xxxxxxxxxx

A Quantum Chemical Model for a Series of Self-Assembled Nanocage: The Origin of Stability Behind the Coordination-Driven Formation of Transition Metal Complexes up to $[M_{12}L_{24}]^{24+}$

Yuichiro Yoshida,[a] Satoru Iuchi,[b] and Hirofumi Sato*[a,c,d]

Received Date
Accepted Date

DOI: 00.0000/xxxxxxxxxx

Herein, we present a systematic computational model to study electronic states and free energies of self-assembled multi-metal complex series. By combining the previously developed model Hamiltonian approach for transition-metal complexes and the generalized Born model, thermodynamics, optimized geometries, electronic states of $[Pd_{12}L_{24}]^{24+}$ nanocage, and $[Pd_nL_m]^{2n+}$ complex series are revealed. The effective model Hamiltonian is a theoretical method to obtain d-electron wavefunction and potential energy including interaction energy between transition-metal and ligands. In the present improvement, the electronic state on each transition-metal center is focused as a building unit and solved under the whole electronic field of the assembling system. We realize a reliable and systematic treatment of multi-transition-metal complexes having different sizes and charges. Consequently, our model could reproduce binding energies of $[Pd_nL_m]^{2n+}$ complex series quantitatively as compared to the density functional theory (DFT). Regarding free energy, we revealed that the assembling solute becomes unstable due to the electrostatic interaction, and effects of the solvent and counter anions mainly compensated it. Optimized geometries were also analysed. The local square-planar coordination structures around the palladium centres were characterized in the complex series. The relationships between entire symmetrical geometries and the local coordination structures are also discussed. Finally, electronic structures of the $[Pd_{12}L_{24}]^{24+}$ nanocage were well characterized as a single-determinant, where only $d_{x^2-y^2}$ is unoccupied due to the ligand-field effect. We also found that the solvent polarized the electronic states of the Pd ions, whereas the counter anion suppressed the polarization. The present method realizes size-independently reliable and rapid computations, and therefore, can be expected to further application studies on self-assembly dynamics.

1 Introduction

Coordination-driven self-assembly creates discrete and highly-charged nanostructures in different sizes in solution.[1–11] Fujita *et al.* reported self-assembled nanocage $[Pd_{12}L_{24}]^{24+}$ and analogues of different sizes composed of similar building blocks, namely palladium(II) and ligand (L).[1–5] How can we understand the mechanism to determine the size of the charged complexes? The key to metal-complex formation is directional coordination bonds, which are derived from multiple configurations of d-electrons. The molecular mechanical (MM) force field is widely used for the computation of large molecules[12–14], but it cannot be used.

Semi-empirical quantum mechanical (QM) approaches, such as density functional tight-binding model (DFTB3), have been applied to transition metals in the past several years,[15,16] but here, we are taking a different approach: An effective model Hamiltonian, which is a semi-empirical QM method, having wavefunctions in a d-orbital space.[17,18] An explicit treatment of the wavefunction for d-electron is essential to understand the directional coordination bond[19]. The similar model Hamiltonian is applied to several transition-metal complex systems and works very well: the potential energies of d–d states of nickel(II) in aqueous solution,[17] those of iron(II)-bipyridine complex,[18,20] and ligand-exchange reaction at a palladium(II) capsule complex.[21] There are two suitable features in the model Hamiltonian. First, the Hamiltonian has some interaction terms between the transition metal centre and ligand environment, which have clear physical meanings. This clarifies how the complex is stable. Second, we treat a multi-metal complex as an assembly of building blocks centred on each transition metal. Therefore, electronic states on each transition metal centre can be focused and solved under the

[a] *Department of Molecular Engineering, Graduate School of Engineering, Kyoto University, Nishikyo-ku, Kyoto 615-8510, Japan. E-mail: hirofumi@moleng.kyoto-u.ac.jp*
[b] *Graduate School of Informatics, Nagoya University, Furo-cho, Chikusa-ku, Nagoya 464-8601, Japan. E-mail: iuchi@i.nagoya-u.ac.jp*
[c] *Elements Strategy Initiative for Catalysts and Batteries (ESICB), Kyoto University, Nishikyo-ku, Kyoto 615-8520, Japan*
[d] *Fukui Institute for Fundamental Chemistry, Kyoto University, Takano Nishihiraki-cho 34-4, Sakyo-ku, Kyoto 606-8103, Japan*

whole assembling system. The increase of the computational cost should be directly proportional to the number of metals, and the reliability is independent of the complex size.

Solvation affects the assembly of charged-complex series. When some complexes assemble, electrostatic interactions between the charges of the same sign make the system unstable. On the contrary, the more charged the complex becomes, the larger is the solute-solvent interaction. The two contributions cancelling out each other is necessary to be treated in a balanced way.[22] In this study, solvation free energy is evaluated using the generalized Born (GB) model.[23–26] The GB is an efficient and reliable solvation model and has been commonly used for solvation of biomolecules.[27,28] Another advantage of the GB is its tractable analytical gradients that are used to obtain stable structures of charged species in solution. Molecular dynamics (MD) simulation and enhanced sampling techniques have been applied to self-assembly in the last four years,[29–32] but performing uniform sampling across various sizes and drastically-changing charges is still challenging. Regarding the three-dimensional reference interaction site model (3D-RISM), Fujita *et al.* carefully applied some correction methods[33–35] to an amphiphilic self-assembling system.[36] It is, however, still unclear whether the approximations in 3D-RISM are suitable for the charged assembling series; furthermore, realizing geometry optimization is challenging.

The stability of the complexes should be discussed based on free energy, not potential energy. Analytical gradients are necessary to perform free energy analysis through geometry optimization and vibrational analysis. Both the model Hamiltonian and GB methods have analytical gradients, and therefore, free energy can be obtained in a stable structure in solution. The entropy terms make an important contribution to self-assembly.[32,37] Overestimation of the vibrational entropy is known as a serious problem owing to the low-lying vibrational frequencies in the harmonic approximation.[38,39] The potential energy surface of a metal complex is relatively flat, and therefore, we carefully compared the free energies by suppressing the overestimation.

To summarize, the present strategy offers size-independent accuracy, rapid computation and a clear view of the electronic structure, thanks to the model Hamiltonian: The electronic structure of the palladium ions under the surrounding environment is well characterised through the valence wavefunction. Besides, it is straightforward to be combined with MD simulation, enabling us to compute a solution system with further sophistication.

In this study, the $[Pd_{12}L_{24}]^{24+}$ nanocage discovered by Fujita *et al.*[1–5] and its partial series $[Pd_nL_m]^{2n+}$ are investigated. As mentioned above, to discuss the thermodynamic stability of charged metal-complexes of different sizes, it is necessary (1) to treat the d-electrons in a QM manner, (2) to estimate the solvation effect for the charged series, and (3) to realize free energy evaluation in a systematic manner. In this study, we propose a systematic computation that considers all the aforementioned points, for the first time. First, we describe the model Hamiltonian that efficiently treats the electronic states of the transition metals and the gradients. Second, the GB model and its parametrization are described. In the result section, first, we show the reliability of our QM model as compared to that of the single-point density functional theory (DFT) calculations. Then, free energy evaluation and geometry optimization results are discussed. Finally, we analyse the electronic states of transition metals in the giant $[Pd_{12}L_{24}]^{24+}$ complex.

2 Computational Methods

In this section, we present a summary of the computational methods used by our model. First, the effective model Hamiltonian developed previously[17,18] and the present extension are described. Second, we briefly describe the GB method and the Hawkins' pairwise approximation[23–25] to obtain reasonable effective Born radii of palladium(II) complexes.

2.1 Model Hamiltonian

In the model Hamiltonian approach, the n-th d–d state energy E_n at given nuclear coordinates $\boldsymbol{R}$ for a palladium(II) centre in a complex is obtained by diagonalizing the model effective Hamiltonian matrix $\boldsymbol{H}_{\rm eff}$ as

$$\boldsymbol{H}_{\rm eff}(\boldsymbol{R})\boldsymbol{C}^{(n)}(\boldsymbol{R}) = E_n(\boldsymbol{R})\boldsymbol{C}^{(n)}(\boldsymbol{R}) \tag{1}$$

where the basis functions of $\boldsymbol{H}_{\rm eff}$ are 45 Slater determinants originating from $4d^8$ electronic configurations $\{\Phi\}$. The wavefunction of the n-th electronic state Ψ_n is written as a linear combination of these Slater determinants as

$$|\Psi_n(\boldsymbol{r};\boldsymbol{R})\rangle = \sum_{I=1}^{45} C_I^{(n)}(\boldsymbol{R})\,|\Phi_I(\boldsymbol{r};\boldsymbol{R})\rangle \tag{2}$$

where $\boldsymbol{r}$ are the metal electronic coordinates. Each Slater determinant $|\Phi(\boldsymbol{r};\boldsymbol{R})\rangle$ is simply composed of Pd^{2+} 4d atomic Slater-type orbitals φ with spin functions, where the exponent ζ_{4d} is a parameter to be determined. In actual calculations, all the orbitals φ are expanded into six Gaussian 3d functions using the reported coefficients and exponents.[40]

The model Hamiltonian matrix $\boldsymbol{H}_{\rm eff}$ is composed of four terms as

$$\boldsymbol{H}_{\rm eff} = \boldsymbol{H}^{\rm Pd^{2+}} + \boldsymbol{H}^{\rm ES} + \boldsymbol{H}^{\rm EX} + \boldsymbol{H}^{\rm CT} \tag{3}$$

The first term describes the electron repulsion in an isolated Pd^{2+} ion. The last three terms describe the metal-ligand electrostatic (ES), exchange (EX), and charge-transfer (CT) interactions. By simply modelling these terms, electronic energies of the transition metal ion under the surrounding environment can be evaluated in a computationally cheap manner via the diagonalization of the model Hamiltonian. By applying this Hamiltonian to each transition metal centre in a complex, the energies and electronic states on each centre can be obtained. The explicit forms of the model Hamiltonian matrix are described as follows.

Isolated Pd^{2+} term: This term is modelled by the Slater integrals F_2 and F_4. The values reported in Ref. 19 are used in this study.

Electrostatic term: We extend the electrostatic interaction matrix elements for the multi-metal complex systems. The ES matrix element between the K- and L-th Slater determinants for the M-th

metal ion is expressed as

$$H_{KL}^{(M),\mathrm{ES}} = \sum_{i(\neq M)}^{N_{\mathrm{atoms}}} \left(\sum_{k,l}^{4\mathrm{d}} \gamma_{kl}^{KL} \left\langle \varphi_k^{(M)} \left| \frac{-Q_i}{|\boldsymbol{r}_M - \boldsymbol{R}_i|} \right| \varphi_l^{(M)} \right\rangle + \frac{Q_i Z_M}{|\boldsymbol{R}_M - \boldsymbol{R}_i|} \delta_{KL} \right) \tag{4}$$

where γ and Q_i are the vector coupling coefficient and the point charge on the i-th atom, respectively. The Z_M is the nuclear charge of the M-th Pd^{2+} ion, which is 10.0e in the present model. In the aforementioned formula, the change of the electronic states on the M-th metal ion is from all other atoms in the system including the other metal ions $M'(\neq M)$. Note that a similar strategy was presented to study ligand-exchange reaction on a local site of a multi-metal complex,[21]; however, the electrostatic field effect from M's was omitted.

Exchange term: The exchange interaction matrix elements for the M-th metal ion are modelled as a product of the overlap integrals:

$$H_{KL}^{(M),\mathrm{EX}} = \sum_{\tilde{m}}^{\mathrm{LMO}} C_{\mathrm{EX}}^{\tilde{m}} \sum_{i}^{\mathrm{NB\ sites}} \sum_{k,l}^{4\mathrm{d}} \gamma_{kl}^{KL} \left\langle \varphi_k^{(M)} | \tilde{m}_i \right\rangle \left\langle \tilde{m}_i \left| \varphi_l^{(M)} \right\rangle \right. \tag{5}$$

where $C_{\mathrm{EX}}^{\tilde{m}}$ are adjustable parameters for the localized molecular orbitals (LMOs), $\tilde{m} = \sigma, \pi$. The LMOs are modelled by atomic 2p orbitals defined in the local frame $\tilde{x}\tilde{y}\tilde{z}$ of binding sites on each ligand. In the present model, the binding sites are nitrogen atoms (NB), and $2p_{\tilde{x}}$ and $2p_{\tilde{z}}$ are used to represent σ and π, respectively; $\tilde{x}$ is parallel to the bisectional line of two NB–CA bonds, and $\tilde{z}$ is normal to the CA–NB–CA plane as shown in Figure 1. The exponent of Slater type atomic orbital for nitrogen, ζ_{2p}, is an adjustable parameter, and the orbital was expanded into six Gaussian 2p functions[41] in evaluating the overlap integrals.

Charge transfer term: The charge transfer interaction matrix elements for the M-th metal ion are introduced by considering charge-transferred configurations from the ligand to the metal 4d and 5s orbitals as

$$H_{KL}^{(M),\mathrm{CT}} = \sum_{i}^{\mathrm{NB\ sites}} C_{\mathrm{CT}}^{\tilde{m}} \sum_{S}^{\mathrm{CTconfig}} \sum_{k,l}^{4\mathrm{d}} (\gamma_S)_{ik}^{KS} \left\langle \tilde{m}_i \left| \varphi_k^{(M)} \right\rangle \right. (\gamma_S)_{li}^{KS} \left\langle \varphi_l^{(M)} \right| \left. \tilde{m}_i \right\rangle$$

$$+ \sum_{i}^{\mathrm{NB\ sites}} E_{\mathrm{CT}}^0 \left[\{1 - \exp(-k_{\mathrm{CT}} \left(|\boldsymbol{R}_M - \boldsymbol{R}_i| - R_{\mathrm{CT}}^0 \right))\}^2 - 1 \right] \delta_{KL} \tag{6}$$

with the vector coupling coefficient:

$$(\gamma_S)_{ik}^{KS} = \left\langle \tilde{m}_i \bar{\tilde{m}}_i \Phi_K \left| \hat{a}_{i\alpha}^\dagger \hat{a}_{k\alpha} + \hat{a}_{i\beta}^\dagger \hat{a}_{k\beta} \right| \tilde{\Phi}_S \right\rangle \tag{7}$$

where $\tilde{\Phi}_S$ are the CT configurations from a ligand occupied orbital to a metal unoccupied 4d orbital and thus originated from $(\tilde{m}_i)^1(\varphi_{4\mathrm{d}})^9$. The operators $\hat{a}^\dagger$ and $\hat{a}$ are creation-annihilation operators. In the present modelling, only the σ type orbital was considered for $\tilde{m}$ to reduce the number of parameters for simplicity as the overlap integrals containing σ are expected to be larger than those containing π, and thus, C_{CT}^{σ} is an adjustable parameter. The second term represents the CT to 5s orbitals, which can be also modelled by the overlap integrals as in the first term by using the 5s orbitals.[17] However, this term contributes only to the diagonal elements, and thus, a simpler modelling by using the Morse potential was employed.[18,42] E_{CT}^0, k_{CT}, and R_{CT}^0 are adjustable parameters.

Energy and Gradients: The ground state energy of multi-metal system is given as

$$E_0^{\mathrm{total}} = \sum_{M}^{N_M} E_0^{(M)} - \sum_{M>M'}^{N_M} \frac{Q_M Q_{M'}}{|\boldsymbol{R}_M - \boldsymbol{R}_{M'}|} + V_{\mathrm{MM}} \tag{8}$$

where N_M is the number of metal and $E_0^{(M)}$ is the ground state energy of M-th metal complex. The $E_0^{(M)}$ is evaluated by diagonalizing the model Hamiltonian for the M-th ion, $\boldsymbol{H}_{\mathrm{eff}}^{(M)}$.

$$\boldsymbol{H}_{\mathrm{eff}}^{(M)} = \boldsymbol{H}^{\mathrm{Pd}^{2+}} + \boldsymbol{H}^{(M),\mathrm{ES}} + \boldsymbol{H}^{(M),\mathrm{EX}} + \boldsymbol{H}^{(M),\mathrm{CT}} \tag{9}$$

Hence, the electronic states and $E_0^{(M)}$ of a metal centre (M) are determined under the ligand-field effects of the whole system including other metals. This procedure is performed for each metal centre, leading to the double-counting of the metal-metal interaction appeared in Eq. (4). This double-counting is then removed as the second term in Eq. (8). The last term of this equation is the contribution from the MM force field, including the intramolecular interactions within each ligand and counter anion BF_4^-, the intermolecular interactions between these species, and non-electrostatic interactions between Pd^{2+} and counter anion. Note that, in the crystal structure of nanocage $[Pd_{12}L_{24}]^{24+}$,[5] metal-metal distances are more than 1 nm; therefore, the influence on the M-th complex from the other metal ions can be considered classically, and the metal-metal dispersion interaction is negligible. The charge of other metals $Q_{M'}$ is set to +2.

The gradient of singlet ground-state energy shown in Eq. (8) with respect to $\boldsymbol{R}_i$ are written as

$$\boldsymbol{G}_i = \sum_{M}^{N_M} \frac{\partial E_0^{(M)}}{\partial \boldsymbol{R}_i} - \sum_{M\neq M'}^{N_M} \frac{\partial}{\partial \boldsymbol{R}_i} \frac{Q_M Q_{M'}}{|\boldsymbol{R}_M - \boldsymbol{R}_{M'}|} + \frac{\partial V_{\mathrm{MM}}}{\partial \boldsymbol{R}_i}, \tag{10}$$

where the first term is obtained from the first derivative of the effective Hamiltonian:[18]

$$\frac{\partial E_0}{\partial \boldsymbol{R}_i} = \sum_{KL} C_K^{(0)} \frac{\partial H_{KL}^{\mathrm{eff}}}{\partial \boldsymbol{R}_i} C_L^{(0)}. \tag{11}$$

Ligand: The general Amber force field (GAFF)[43] was employed as the potential function for describing the ligand and the interactions between them.

2.2 Generalized Born model

The solvation free energy G_{GB} is estimated using the GB model:[23,26]

$$G_{\mathrm{GB}} = -\frac{1}{2}\left(1 - \frac{1}{\varepsilon}\right) \sum_{i,j}^{N_{\mathrm{atoms}}} \frac{Q_i Q_j}{\eta_{\mathrm{GB}}} \tag{12}$$

$$\eta_{\mathrm{GB}} = \left[R_{ij}^2 + \alpha_i \alpha_j \exp\left(-\frac{R_{ij}^2}{4\alpha_i \alpha_j} \right) \right]^{1/2} \tag{13}$$

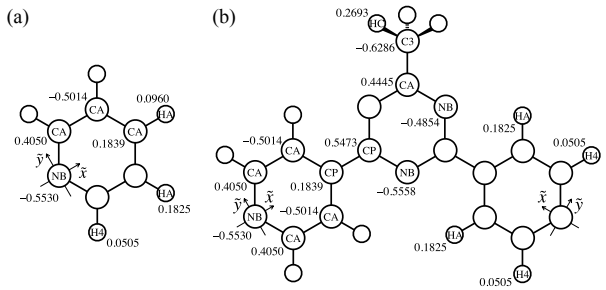

Fig. 1 Atom types and point charges of (a) pyridine and (b) bidentate ligand L. Only the parameters of symmetrically unique atoms are shown. Definition of the local frame $\tilde{x}\tilde{y}\tilde{z}$ on the binding sites is also displayed.

where ε, α_i, and R_{ij} are the dielectric constant, effective Born radius of i-th atom, and distance between atoms i and j, respectively. The value of ε was set to 46.7, corresponding to the relative dielectric constant of dimethylsulfoxide (DMSO).[5] The determination of the effective Born radius α is an important factor for a reliable estimation of solvation free energy. However, to the best of our knowledge, few case studies for transition metal complex exist; therefore, to reproduce the solvation free energy of polarizable continuum model (PCM), we performed parametrization for the building unit centred on metal.[44,45]

The effective Born radii, α, in Eq. (13), can be determined by the pairwise approximation developed by Hawkins *et al.*[24–26] as

$$\alpha_i^{-1} = \rho_i^{-1} - \frac{1}{2}\sum_j \left(\frac{1}{L_{ij}} - \frac{1}{U_{ij}} + A_{ij} + B_{ij} \right) \tag{14}$$

$$A_{ij} = \frac{R_{ij}}{4}\left(\frac{1}{U_{ij}^2} - \frac{1}{L_{ij}^2} \right) \tag{15}$$

$$B_{ij} = \frac{1}{2R_{ij}} \ln \frac{L_{ij}}{U_{ij}} + \frac{S^2\rho_j^2}{4R_{ij}}\left(\frac{1}{L_{ij}^2} - \frac{1}{U_{ij}^2} \right) \tag{16}$$

$$L_{ij} = U_{ij} = 1 \quad \text{if} \quad R_{ij} + S\rho_j \le \rho_i \tag{17}$$

$$L_{ij} = \rho_i \quad \text{if} \quad R_{ij} - S\rho_j \le \rho_i \le R_{ij} + S\rho_j \tag{18}$$

$$L_{ij} = R_{ij} - S\rho_j \quad \text{if} \quad \rho_i \le R_{ij} - S\rho_j \tag{19}$$

$$U_{ij} = R_{ij} + S\rho_j \quad \text{if} \quad \rho_i \le R_{ij} + S\rho_j \tag{20}$$

where ρ_i is the intrinsic radius of the i-th atom. S is a scale factor of ρ, which is introduced to reduce overestimation of effective Born radii α,[24,25] and various S values have been prepared according to the pair of atom types. In this study, however, for simplicity, one constant value was introduced regardless of atom pairs.

3 Parametrization

3.1 Parametrization for model Hamiltonian

The bidentate ligand L in $[Pd_{12}L_{24}]^{24+}$ has two pyridine (py) rings that coordinate to metal ions individually (Figure 1); therefore, the interactions between Pd^{2+} and L at these pyridine binding regions were focused to determine the parameters in the model Hamiltonian. Specifically, the *ab initio* electronic structure calculation results for the $[Pd(py)_4]^{2+}$ complex were used as reference data.

Point charges of ligand: The point charges on ligand atoms were determined by the restrained electrostatic potential (RESP) fits[46] to be consistent with GAFF utilized for the ligand term in Eq. (8). To include the polarization effect between the ligands effectively, the RESP charges were determined from the $(py)_4$ structure without the Pd^{2+} ion. The $(py)_4$ structure was obtained from the $[Pd(py)_4]^{2+}$ structure optimized by MP2 with Stuttgart/Dresden (SDD) ECP[47] for Pd and 6-311G*[48] basis set for other atoms. The Merz-Singh-Kollman scheme[49,50] was employed to generate grid points. The RESP fitting was performed at the HF/6-31G* level using the *Antechamber* program.[51] The resultant RESP charges are summarized in Figure 1(a) with the atom types for GAFF.

For the bidentate ligand L, the same point charges Q were used at the two pyridine rings in L except for HA atom at the opposite side from the ligating NB, as shown in Figure 1(b). The charges on the two HA atoms were redistributed to the remaining region of L to conserve charge neutrality based on the Mulliken charges determined for L. The Mulliken charges were determined by the HF/6-311G* level at the MP2-optimized structure.

Fitting procedure: The genetic algorithm[52] was used to determine the parameters by minimizing a function

$$\chi^2 = \sum_i^{N_{\text{config}}} e^{-w(E_i^{\text{MP2}} - E_0^{\text{MP2}})} (E_i^{\text{model}} - E_i^{\text{MP2}})^2 \tag{21}$$

where E_0^{MP2} is the ground state energy at the optimized structure $\boldsymbol{R}_0$ at the MP2 level. Through this fitting, the metal-ligand dispersion interaction is effectively taken into account in the model Hamiltonian. E_i^{MP2} is the MP2 energy at the structure $\boldsymbol{R}_i = \boldsymbol{R}_0 \pm \boldsymbol{q}_n$, where $\boldsymbol{q}_n$ is the n-th normal mode. The 16 normal modes corresponding to the lowest 16 frequencies were chosen, because these soft modes correspond to relative pyridine-ring motions around the heavy Pd^{2+} ion and are important to reproduce coordinate bonds. The number of structures employed, N_{config}, were 33 in total, including $\boldsymbol{R}_0$. The weight w was set to 10.0 Hartree^{-1}. The obtained parameters are summarized in Table 1.

Potential energy surface properties of $[Pd(py)_4]^{2+}$: As a result of the fitting of potential energy curves along with low-frequency normal modes, the model Hamiltonian reproduced those of the MP2 calculations quantitatively. In this part, the optimized structures of $[Pd(py)_4]^{+2}$ and normal-mode frequencies are compared.

A good description around the optimized structure is manifested in correspondence with $[Pd(py)_4]^{+2}$ structures optimized by the model Hamiltonian, and the MP2 calculation as summarized in Table 2. Geometry optimization of the model was performed using the L-BFGS minimizer[53,54] in OPTIM,[55] and the convergence criterion for the root-mean-square gradient was 5.0×10^{-6}. Both the structures are D_4 symmetrical, and the differ-

Table 1 Parameters in the model Hamiltonian

	Parameter	Unit
F_2	1200.3[a]	cm^{-1}
F_4	74.9[a]	cm^{-1}
ζ_{4d}	2.9286	a.u.
ζ_{2p}	4.3744	a.u.
C^{σ}_{EX}	45.3715	a.u.
C^{π}_{EX}	82.9277	a.u.
C^{σ}_{CT}	0.5904	a.u.
E^{0}_{CT}	49.1065	kcal/mol
k_{CT}	3.2796	$Å^{-1}$
R^{0}_{CT}	1.9599	Å

(*a*) Taken from Ref. 19.

ence of the Pd–N bond length is less than 0.01 Å. The differences in Pd–N–C bond angle and N–Pd–N–C dihedral angle are within 2.3°.

Table 2 $[Pd(py)_4]^{2+}$ structures optimized by the model Hamiltonian and MP2

	Pd–N (Å)	Pd–N–C (°)	N–Pd–N–C (°)[b]
Model	2.04	122.6	123.1
MP2[a]	2.04	120.3	124.4

(*a*) Stuttgart/Dresden ECP[47] for Pd and 6-311G*[48] basis set for other atoms.
(*b*) Two N atoms belong to two adjacent ligands.

Figure 2 displays the comparison of the normal mode frequencies between the model Hamiltonian and MP2 calculations. Each red circle corresponds to a normal mode that was assigned using the absolute value of the inner product of normal mode vectors, $|\boldsymbol{q}_{\mathrm{Model}} \cdot \boldsymbol{q}_{\mathrm{MP2}}|$. As seen in Figure 2, the normal mode frequencies up to 1000 cm^{-1} are in a good agreement, though only 16 normal modes up to roughly 200 cm^{-1} were employed for the parameter fitting. Note that the modes with relatively large frequency (∼1000 cm^{-1} and more) are characterized by intramolecular vibration in ligand, and thus, are mostly characterized by the quality of GAFF employed for the ligand.

3.2 Parameter for generalized Born model

The intrinsic radii $\{\rho_i\}$ are 1.63, 1.47, 1.70, 1.55, 1.92, and 1.20 Å for Pd, F, C, N, B, and H, respectively.[56,57] A scale factor, $S = 0.863$, was introduced regardless of atom pairs for simplicity. This value was determined in order to reproduce the solvation free energies of $[Pd_3L_9(BF_4)_6]$ and $[Pd_2L_7(BF_4)_4]$, and these partial structures $[PdL_4(BF_4)_2]$s and Ls obtained by PCM[44,45] by fitting, where these structures were taken from the crystal structure of $[Pd_{12}L_{24}(BF_4)_{24}]$.[5] We confirmed the differences of the solvation free energies were also reproduced quantitatively. The PCM calculation was performed at the M06L[58] level with LANL2DZ ECP[59] for Pd and 6-31G* basis set[60,61] for other atoms using the GAMESS program.[62]

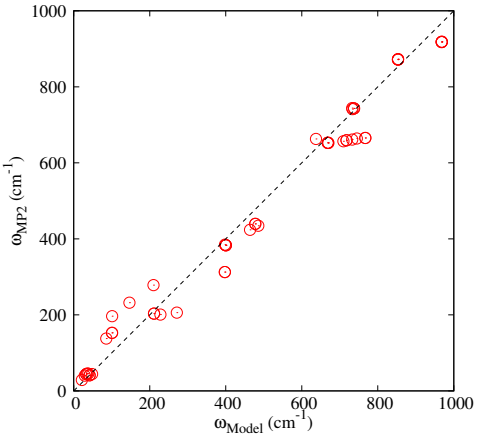

Fig. 2 Normal mode frequencies of the model Hamiltonian and MP2.

4 Results and discussion

4.1 Comparison of model Hamiltonian and DFT using binding energy

Our first goal is to develop an effective QM model to describe assembled metal-complex series $[Pd_nL_m]^{2n+}$ with different sizes and charges. Here, to discuss the reliability of our model, single-point binding energies were compared to those of DFT at the crystal and its partial structures. The binding energy ΔE of $[Pd_nL_m]^{2n+}$ complex was evaluated by the following equations:

$$n\mathrm{PdL_4} \rightarrow \mathrm{Pd}_n\mathrm{L}_m + (4n-m)\mathrm{L} \tag{22}$$

$$\Delta E = E(\mathrm{Pd}_n\mathrm{L}_m) + (4n-m)E(\mathrm{L}) - nE(\mathrm{PdL_4}) \tag{23}$$

where the integers n and m represent the numbers of Pd^{2+} and L in the complex, respectively. Here, each palladium is assumed to form four coordinate bonds with Ls, and six complexes of $(n,m) = (1,4),(2,7),(3,9),\ (4,12),\ (5,14)$, and $(12,24)$ were prepared from the crystal structure of $(12,24)$.[5] Among them, ΔE for $(2,7)$ and $(3,9)$ were computed with different basis sets and DFT functionals to assess the dependency (Table 3). ΔE was different in several kcal/mol for both complexes. Compared to the computations with the largest set, the differences are 3-4% and 7% for M06-L and M06-2X, respectively. Hence, it could be said that the basis set dependencies are not significant in both functionals.

Table 4 lists ΔEs for the series of complexes with the present model Hamiltonian. In Figure 3, ΔE is plotted with respect to the complex size n. The ΔE increases rapidly as the system size becomes large. This is rationalized by considering that the complex $[Pd_{12}L_{24}]^{24+}$ forms the cage-like structure including twelve Pd^{2+} ions, and the large instability is due to unfavourable ES interactions between positive ions. To see this further, we confirmed that the expected value of ES increases as the complex becomes large, whereas, those of EX and CT do not by the construction of the model Hamiltonian.

The DFT results computed with the two functionals at the same

Table 3 Basis set dependence of the energies ΔE

method	$(2,7)$	$(3,9)$
M06-L[63,64]		
LANL2DZ, 6-31G*	96.1 (−4.1 %)	276.3 (−3.8 %)
SDD, 6-31G*	96.8 (−3.3 %)	277.6 (−3.3 %)
SDD, 6-311G*	100.1 (0.0 %)	286.8 (0.0 %)
M06-2X[63,64]		
LANL2DZ, 6-31G*	93.6 (−6.9 %)	272.1 (−6.9 %)
SDD, 6-31G*	93.5 (−6.9 %)	272.1 (−7.0 %)
SDD, 6-311G*	100.0 (0.0 %)	291.0 (0.0 %)

Energies are in kcal/mol, and the difference with respect to the 6-311G* values are in the parenthesis.

geometry and the difference from them are also shown in the table. The agreements are sufficient for all the complexes within a few percents, i.e. independent to the size. For $(2,7)$ and $(3,9)$, the differences are smaller than those from the basis set dependency shown in Table 3, indicating that the present model is well-designed.

Table 4 Single-point binding energies ΔE of $[Pd_nL_m]^{2n+}$ series (kcal/mol)

(n,m)	Model	M06-L[a]	M06-2X[a]
$(2,7)$	96.5 (0.4 %, 3.2 %)	96.1	93.6
$(3,9)$	282.0 (2.0 %, 3.6 %)	276.3	272.1
$(4,12)$	514.1 (1.0 %, 1.6 %)	509.2	505.8
$(5,14)$	809.5 (2.0 %, 1.7 %)	793.8	796.3
$(12,24)$	4724.7 (−0.3 %, 1.5 %)	4739.0	4654.6

(*a*) LANL2DZ ECP for Pd and 6-31G* basis set for other atoms were used. Energies are in kcal/mol, and the differences between the model and the references (M06-L and M06-2X) are in the parenthesis, respectively.

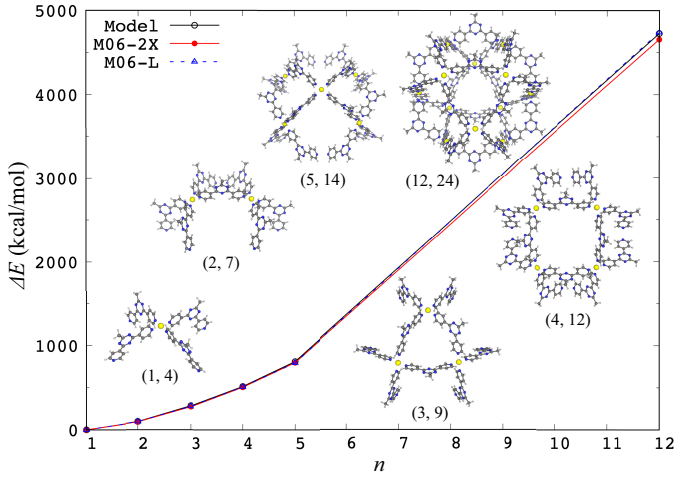

Fig. 3 Single-point binding energies of complexes $[Pd_nL_m]^{2n+}$, ΔE (Eq. (23)), from the model Hamiltonian (black open circles), M06-2X calculations (red filled circles), and M06-L calculations (blue open triangles). LANL2DZ ECP for Pd and 6-31G* basis set for other atoms were used. Structures of the complexes are also shown.

4.2 Estimation of free energies in solution

Free energy estimation was performed by combining the model Hamiltonian and GB. All of the supramolecules (n,m) were optimized at three conditions: in gas phase, solution phase, and solution phase with BF_4^-s.

The binding energy ΔE of $[Pd_nL_m]^{2n+}$, solvation free energy difference $\Delta\delta G_{GB}$ for the $[Pd_nL_m]^{2n+}$ formation, interaction energy ΔE_{int} between $[Pd_nL_m]^{2n+}$ and $2nBF_4^-$, and the configurational entropic term $-T\Delta S$ were examined as follows.

$$\Delta G_{sum} = \Delta E + \Delta\delta G_{GB} + \Delta E_{int} - T\Delta S \tag{24}$$

where T denotes the temperature (298.15 K) and δ represents the structural relaxation by the solvent effect. The thermodynamic cycle to estimate the stability of $[Pd_nL_m]^{2n+}$ is shown in Scheme 1. The interaction energy is the energy difference of the optimized structures between with and without BF_4^- as follows.

$$\Delta E_{int} = E([Pd_nL_m(BF_4)_{2n}]) + G_{GB}([Pd_nL_m(BF_4)_{2n}])$$
$$- \left[E([Pd_nL_m]^{2n+}) + G_{GB}([Pd_nL_m]^{2n+}) + 2n\left\{E(BF_4^-) + G_{GB}(BF_4^-)\right\}\right]. \tag{25}$$

The configurational entropy term is evaluated using rigid-rotor harmonic-oscillator approximation.[65] Geometry optimization was performed using the L-BFGS algorithm[53,54] in OPTIM,[55] and the convergence criterion for the root-mean-square gradient was 5.0×10^{-6}. The crystallographic information was used for the initial guess. To reveal the size and environmental effects, only local optimizations were performed. Regarding BF_4^-, the force field parameters developed by Liu *et al.* were used.[66] Lennard-Jones potential parameters for Pd were introduced to describe Pd–BF_4 binding, that is, $\sigma = 4.74$ Å and $\varepsilon = 0.027$ kcal/mol. The former was determined from the MM3 atomic size,[67] and the latter from fitting. Note that the fitting value is extremely close to the value from the Mavroynnis–Stephen theory with atomic polarizability.[68–70] The vibrational entropies were estimated through normal-mode analysis with a correction method for low-lying frequency modes developed by Grimme.[39] Second derivatives of the model Hamiltonian and GB were calculated in a semi-analytical manner.

Table 5 presents the computed free energies and their components in Eq. (24). The binding energies ΔE are positive for all the $[Pd_nL_m]^{2n+}$ complexes and increase with the increase in the system size, as discussed on the single-point comparison in Section 4.1. In contrast, the solvation free energy differences and the interaction energies with anions are all negative and their absolute values increase with the increase in the size of the system. For larger complexes, ΔE becomes large and is almost compensated by $\Delta\delta G_{GB}$. ΔE_{int} is the second leading term to compensate unfavourable ΔE, although different from $\Delta\delta G_{GB}$ by an order of magnitude. One might wonder if BF_4^-s are bound or not. One of the reasons why BF_4^- was assumed to be bound is that the anomaly highly-charge of the metal-complex, up to +24. The charge of the smallest one ($n=2$) is +4, but the anion should be bound to make comparison uniformly over the com-

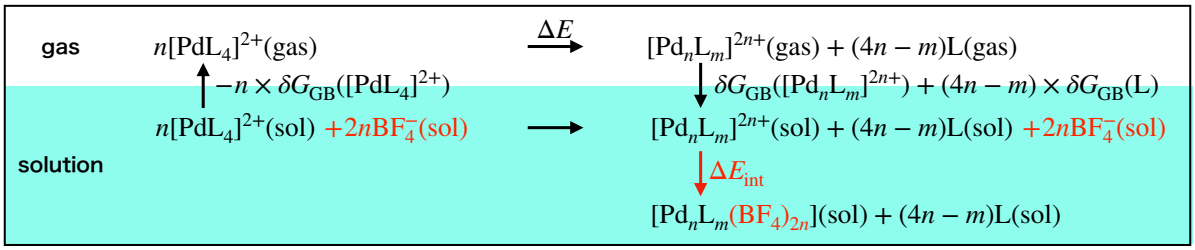

Scheme 1 Thermodynamic cycle to estimate the stability of $[Pd_nL_m]^{2n+}$.

Table 5 Free energy components in Eq. (24) for $[Pd_nL_m]^{2n+}$ (kcal mol^{-1})

(n, m)	ΔE	$\Delta\delta G_{GB}$	ΔE_{int}	$-T\Delta S_{trans}$	$-T\Delta S_{rot}$	$-T\Delta S_{vib}$	ΔG_{sum}
(2, 7)	38.8	−36.0	−37.3	0.8	0.1	−0.5	−34.2
(3, 9)	273.8	−262.7	−59.6	−8.9	−8.4	9.2	−56.5
(4, 12)	405.7	−390.2	−82.8	−7.8	−6.9	11.8	−70.2
(5, 14)	709.4	−690.1	−110.0	−17.4	−15.2	24.5	−98.8
(12, 24)	4537.2	−4395.9	−313.4	−127.0	−113.5	126.8	−285.8

plexes. In our computations, the solution system can be electrically neutral by explicitly introducing the anions into the system. This treatment may be supported by a cold-spray ionization mass spectrometry (CSI-MS)[71,72] experiment where there were species with different charges $[Pd_{12}L_{24}(BF_4)_{24-l}]^{l+}$ (where l is integer from 11 to 16).[5] It is also noted that, in the crystal structure of $[Pd_{12}L_{24}(BF_4)_{24}]$, the averaged value of the Pd–B distances is 4.37 Å, and that in the present optimized structure is also 4.37 Å.

The contributions of entropic terms are relatively smaller than the solvation free energies by an order of magnitude, but not negligible at all. Because many ligands are released on the binding, the total translational and rotational entropies contribute to the stabilization, in particular of the huge complex like (12, 24), while the vibrational one destabilises it (Table 5). Note that the tendency for the instability of vibrational entropy term does not change without the corrections for low-frequency modes. The entropic terms together make the cage complex stable, and it can be considered that this causes the release of many ligands during the closed $[Pd_{12}L_{24}]^{24+}$ complex formation.

4.3 Optimized geometries

Figure 4 and Table 6 show the optimized geometries of $[Pd_nL_m]^{2n+}$ series in the gas phase, solution phase, and solution phase with BF_4^-s. Overall, structural differences between with and without BF_4^-s in the solution phase is insignificant as the root-mean-square deviation (RMSD) values show (Table 6). However, the gas-phase structures of $n = 2, 4, 5$ complexes are different from the ones in the solution-phase (the RMSDs are 4.868, 5.059, 6.169 Å, respectively). In these complexes, the ligands are stacked with each other due to dispersion interaction, which is included in the GAFF potential. Morever, in the solution-phase results, few $\pi-\pi$ stacking were found between the ligands, owing to the solvent effect.

The local coordination structure around each palladium centre retains the so-called square planar structure, and the averaged values of the bond lengths r_{ave}(Pd–N), bond angles θ_{ave}(Pd–N–C), and dihedral angles ϕ_{ave}(N–Pd–N–C) are listed in Table 6. Only the $[Pd_2L_7]^{4+}$ complex in gas has a five coordinated centre (Figure 4 (b)). Four ligands bind to form a square planer structure, and additionally, one axial site is coordinated by the ligand whose another binding site coordinates to another palladium centre.

The values of r_{ave}(Pd–N), θ_{ave}(Pd–N–C), and $\sin\phi_{ave}$(N–Pd–N–C) are similar in all the cases, but the those of ϕ_{ave}(N–Pd–N–C) have large standard deviations. This is derived from the local coordination structure around each palladium centre. Table 7 presents the averaged trigonometric functions of the dihedral angle $\phi_{ave,M}$(N–Pd–N–C) in each metal centre at $[Pd_{12}L_{24}]^{24+}$. Half of the metal centres have $\cos\phi_{ave}$(N–Pd–N–C) of the opposite sign, and all of the metal centres have $\sin\phi_{ave}$(N–Pd–N–C) of the same sign. The difference is derived from the orientation of the coordinated rings (Figure 5): half of the rings have a clockwise coordination and the remaining half have an anti-clockwise coordination to form S_6 and C_i symmetrical structures in the gas and solution phases, respectively.

Finally, the relationships between optimized geometries and local coordination structures are discussed. Figure 6 classifies the Pd(II) ion centres using color following the local coordination features presented in Table 7. In the gas-phase structure, the two sets of the Pd centres, $(1,10,12)$ and $(2,9,11)$, which have clockwise and anti-clockwise local coordination, respectively, are in the top and bottom positions and form two triangles. In the middle of the cage complex, the two kinds of local coordination structures are alternately arranged in the hexagon ring consisting of the centres $(3,5,7,4,6,8)$. There is a C_3 rotational axis which passes through the centre of the two triangles and hexagon, and a mirror plane on the hexagon ring. A S_6 operation permutes the sets $(1,10,12)$ and $(9,11,2)$ and rotates the set $(3,5,7,4,6,8)$ to $(5,7,4,6,8,3)$ with inversion of the local coordination structures. On the other hand, in the solution phase, the centres in the triangles do not have the same local coordination features. Consequently, the C_3 rotational axis disappears, and the only inversion operation remains. In the BF_4^- binding case in the solution phase, though the

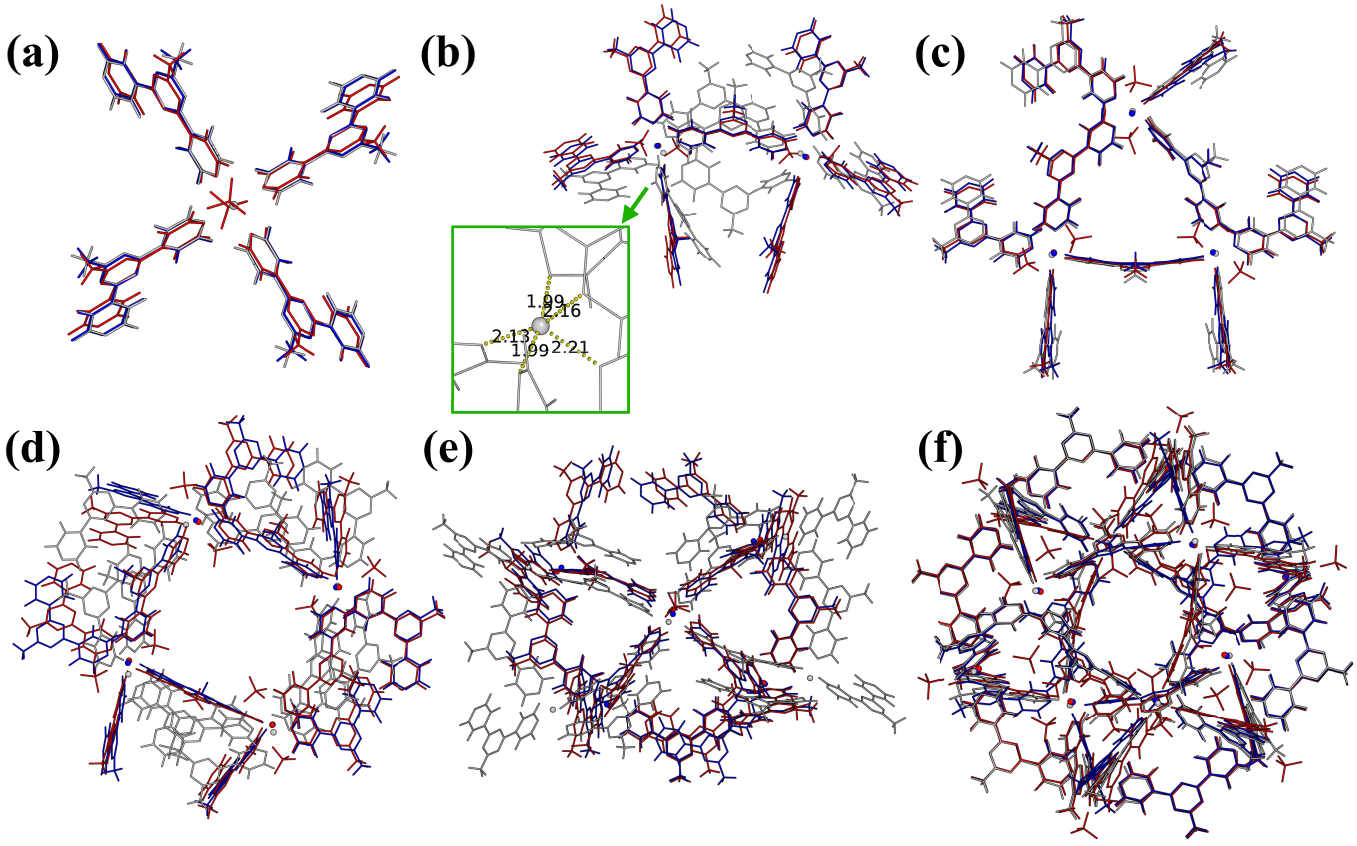

Fig. 4 oOptimized structures of $[Pd_nL_m]^{2n+}$ series; (a) $[PdL_4]^{2+}$, (b) $[Pd_2L_7]^{4+}$, (c) $[Pd_3L_9]^{6+}$, (d) $[Pd_4L_{12}]^{8+}$, (e) $[Pd_5L_{14}]^{10+}$, and (f) $[Pd_{12}L_{24}]^{24+}$. Gray, blue, and red skeletons correspond to those in gas phase, in solution phase, and in solution phase with BF_4^-, respectively.

Table 6 Optimized structures and geometrical properties in each condition

	condition	r_{ave}(Pd–N) (Å)	θ_{ave}(Pd–N–C) (°)	ϕ_{ave}(N–Pd–N–C) (°)[a]	$(\sin\phi)_{ave}$	Point group[b]	RMSD from solution (Å)
$[Pdpy_4]^{2+}$	gas	2.04	122.6	123.1	0.84	D_4	0.068 (from MP2)
	gas (MP2[c])	2.04	120.3	124.4	0.83	D_4	
$[PdL_4]^{2+}$	gas	2.04 ± 0.00	122.7 ± 1.1	124.8 ± 0.4	0.82 ± 0.00	C_4	0.310
	solution	2.06 ± 0.00	123.2 ± 0.0	125.0 ± 0.0	0.82 ± 0.00	C_4	
	solution with $2BF_4^-$	2.05 ± 0.03	122.7 ± 0.1	116.1 ± 0.9	0.90 ± 0.01	C_1	0.371
$[Pd_2L_7]^{4+}$	gas	2.07 ± 0.08	120.9 ± 4.3	89.1 ± 35.4[d]	0.82 ± 0.20	C_1	4.868
	solution	2.06 ± 0.01	123.2 ± 0.3	90.2 ± 34.8	0.82 ± 0.01	C_1	
	solution with $4BF_4^-$	2.05 ± 0.04	122.8 ± 1.3	87.3 ± 29.7	0.87 ± 0.03	C_1	0.509
$[Pd_3L_9]^{6+}$	gas	2.04 ± 0.00	122.8 ± 3.3	96.5 ± 31.6	0.90 ± 0.19	C_1	0.904
	solution	2.06 ± 0.01	123.1 ± 1.0	98.9 ± 30.3	0.85 ± 0.06	C_1	
	solution with $6BF_4^-$	2.05 ± 0.03	122.7 ± 0.5	96.4 ± 22.5	0.92 ± 0.04	C_1	0.372
$[Pd_4L_{12}]^{8+}$	gas	2.05 ± 0.06	119.9 ± 7.2	97.8 ± 26.2	0.89 ± 0.13	C_1	5.059
	solution	2.06 ± 0.02	123.1 ± 1.2	75.6 ± 28.4	0.85 ± 0.07	C_1	
	solution with $8BF_4^-$	2.05 ± 0.04	122.7 ± 1.2	80.9 ± 24.0	0.90 ± 0.06	C_1	1.275
$[Pd_5L_{14}]^{10+}$	gas	2.04 ± 0.05	120.7 ± 6.7	84.9 ± 26.2	0.89 ± 0.08	C_2	6.169
	solution	2.06 ± 0.03	123.1 ± 1.7	83.7 ± 29.4	0.87 ± 0.07	C_1	
	solution with $10BF_4^-$	2.05 ± 0.04	122.6 ± 1.9	84.0 ± 24.7	0.90 ± 0.07	C_1	0.939
$[Pd_{12}L_{24}]^{24+}$	gas	2.05 ± 0.04	123.1 ± 1.0	90.0 ± 22.3	0.93 ± 0.05	S_6	0.909
	solution	2.06 ± 0.01	123.1 ± 1.5	90.0 ± 26.3	0.90 ± 0.06	C_i	
	solution with $24BF_4^-$	2.05 ± 0.04	122.7 ± 1.3	90.0 ± 22.1	0.93 ± 0.05	C_1	1.183
	crystal[5]	2.00 ± 0.03	121.4 ± 1.3	90.0 ± 5.9	0.99 ± 0.01	C_i (without BF_4^-)	1.129

(*a*) Two N atoms belong to two adjacent ligands.
(*b*) Symmetries were determined by SYMMOL.[73] A constant tolerance, 0.005, was used.
(*c*) Stuttgart/Dresden ECP for Pd and 6-311G* basis set for other atoms.
(*d*) The average value around the ligands in the equatorial positions.

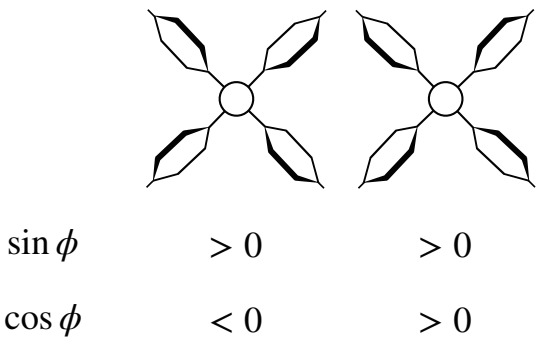

Fig. 5 Local coordination structures and dihedral angle ϕ. Clockwise (left) and anti-clockwise (right).

symmetry is broken, the structural feature is close to the solution-phase structure. The signs of $(\cos\phi)_{\mathrm{ave},M}$ (where $M = 9, 10$) as presented in Table 7 are opposite from those of the gas phase; therefore, the C_3 rotational axis disappears. The value of RMSD from the gas-phase structure is 0.838 Å, which is slightly smaller than that from the solution-phase structure (1.183 Å) and that between the gas- and solution-phase structures (0.909 Å). All the optimized structures and the crystal structure are geometrically close each other.

4.4 Analysis of electronic states of Pd^{2+} ions

Finally, the electronic structure of each palladium(II) ion in $[Pd_{12}L_{24}]^{24+}$ were analysed. The ground state wavefunction of the M-th Pd^{2+} ion was found to be composed of a few Slater determinants at most as

$$\begin{aligned}\left|\Psi_0^{(M)}(\boldsymbol{r}_M;\boldsymbol{R})\right\rangle &= \sum_{I=1}^{45} C_I^{(0,M)}(\boldsymbol{R})\left|\Phi_I^{(M)}(\boldsymbol{r}_M;\boldsymbol{R})\right\rangle \\ &\approx C_1^{(0,M)}(\boldsymbol{R})\,|\xi\bar{\xi}\eta\bar{\eta}\zeta\bar{\zeta}u\bar{u}\rangle + C_2^{(0,M)}(\boldsymbol{R})\,|\xi\bar{\xi}\eta\bar{\eta}\zeta\bar{\zeta}\bar{u}v\rangle \\ &+ C_3^{(0,M)}(\boldsymbol{R})\,|\xi\bar{\xi}\eta\bar{\eta}\zeta\bar{\zeta}u\bar{v}\rangle + C_4^{(0,M)}(\boldsymbol{R})\,|\xi\bar{\xi}\eta\bar{\eta}\zeta\bar{\zeta}v\bar{v}\rangle \\ &+ C_5^{(0,M)}(\boldsymbol{R})\,|\xi\bar{\xi}\zeta\bar{\zeta}u\bar{u}v\bar{v}\rangle \end{aligned} \tag{26}$$

where the abbreviations ξ, η, ζ, u, and v denote five 4d orbitals $\varphi_{yz}^{(M)}$, $\varphi_{zx}^{(M)}$, $\varphi_{xy}^{(M)}$, $\varphi_{z^2}^{(M)}$, and $\varphi_{x^2-y^2}^{(M)}$, respectively. In analyzing $C^{(0)}$, the whole complex was rotated such that the M-th ion was placed at the origin on the local xyz frame, where the x axis was parallel to an arbitral Pd–N bond and the z axis was normal to the N1–M–N2 plane and directed toward the outside of the cage.

As presented in Table 8, the weights $(C_1^{(0)})^2$ are roughly 86 to 96 % for all the Pd^{2+} ions, thereby indicating that the electronic ground states of all the Pd^{2+} ions in $[Pd_{12}L_{24}]^{24+}$ are dominated by a single configuration. This electronic feature is qualitatively the same in all the three structures. This dominant configuration is rationalized by considering the ligand-field theory,[74] where only $\varphi_{x^2-y^2}$ is unoccupied due to repulsion from four ligands in the xy plane for the square-planar transition-metal complex. The weights $(C_1^{(0)})^2$ increase due to the solvation effect and then decrease due to the bound BF_4^-. This result indicates the solvent polarizes the Pd ions and the anions suppress the polarization effect. In this regard, it is concluded that the present model provides a reasonable electronic ground state structure of $[Pd_{12}L_{24}]^{24+}$.

5 Conclusions

A systematic semi-empirical QM model to study the thermodynamics and electronic states of $[Pd_{12}L_{24}]^{24+}$ and $[Pd_nL_m]^{2n+}$ partial series is presented. Our QM model is based on the model Hamiltonian developed previously for d–d states of a transition-metal centre[17,18] with the present improvement to treat the entire field of the supramolecule. Electronic state on each transition-metal centre can be focused and solved under the whole assembling system, and as such, the model reliability is independent of the complex size. Consequently, our model successfully reproduced the binding energies of $[Pd_nL_m]^{2n+}$ series.

Free energies of $[Pd_nL_m]^{2n+}$ series were estimated by combining the model Hamiltonian and GB model. The computed binding energies indicated that the $[Pd_nL_m]^{2n+}$ complex series were quite unstable without the solvation effects owing to the unfavourable electrostatic interactions in the highly charged system. It was also found that the solvation free energies and interactions with counter anions compensated the unfavourable solute binding energies. The entropic contribution was smaller than the binding energy and solvation free energy by an order of magnitude but made the $[Pd_nL_m]^{2n+}$ stable.

Furthermore, optimized geometries in the gas and solution phases were different. The $[Pd_2L_7]^{4+}$, $[Pd_4L_{12}]^{8+}$, and $[Pd_5L_{14}]^{10+}$ complexes in gas phase have $\pi-\pi$ stacking between ligands and retain the square-planer coordination structure. However, in the solution phase, few stacking structures were found and the effect of BF_4^- on the optimized structures was insignificant. In $[Pd_{12}L_{24}]^{24+}$, half of the local coordination structures around each Pd^{2+} centre have clockwise coordination, and the remaining half have anti-clockwise coordination. The relationships between the optimized geometries, which have S_6 and C_i symmetries in the gas and solution phases, respectively, and the local coordination structures, were revealed.

Finally, the electronic character of $[Pd_{12}L_{24}]^{24+}$ was found to be consistent with that of the typical square-planar complex of the d^8 transition-metal ion system. The weights of the ground electronic states indicate that solvation polarizes the Pd ions, whereas, the anions suppress the polarization effect. Giving a clear picture of the electronic structure is an advantage of introducing valence d-electron wavefunctions.

Again, our computational model is focused on the transition metals as building units and can solve the electronic states under the whole assembling system. This feature enables a reliable and systematic study of electronic states and thermodynamics of the charged complex series of different sizes. The present model can be applied to several huge multi-metal complexes without drastically increasing the computational cost. The size-independent accuracy and the ability of rapid computation are suitable features for further studies on coordination-driven self-assembly. Understanding the details of the self-assembly process is an important

Table 7 Characterization of local coordination structures by dihedrals in $[Pd_{12}L_{24}]^{24+}$, where two N atoms belong to two adjacent ligands

M	gas		solution		solution with BF_4^-	
	$(\sin\phi)_{\mathrm{ave},M}$	$(\cos\phi)_{\mathrm{ave},M}$	$(\sin\phi)_{\mathrm{ave},M}$	$(\cos\phi)_{\mathrm{ave},M}$	$(\sin\phi)_{\mathrm{ave},M}$	$(\cos\phi)_{\mathrm{ave},M}$
1	0.94 ± 0.04	-0.30 ± 0.14	0.93 ± 0.07	-0.33 ± 0.16	0.94 ± 0.04	-0.33 ± 0.12
2	0.95 ± 0.03	0.30 ± 0.10	0.93 ± 0.07	0.33 ± 0.16	0.93 ± 0.04	0.33 ± 0.11
3	0.90 ± 0.06	-0.40 ± 0.14	0.93 ± 0.03	-0.35 ± 0.08	0.93 ± 0.04	-0.34 ± 0.12
4	0.91 ± 0.03	0.41 ± 0.06	0.94 ± 0.02	0.35 ± 0.04	0.94 ± 0.04	0.33 ± 0.11
5	0.91 ± 0.03	0.41 ± 0.06	0.89 ± 0.05	0.43 ± 0.09	0.87 ± 0.06	0.48 ± 0.11
6	0.90 ± 0.06	-0.40 ± 0.14	0.89 ± 0.05	-0.43 ± 0.11	0.86 ± 0.07	-0.48 ± 0.14
7	0.90 ± 0.06	-0.40 ± 0.14	0.86 ± 0.05	-0.51 ± 0.09	0.95 ± 0.02	-0.30 ± 0.08
8	0.91 ± 0.03	0.41 ± 0.06	0.86 ± 0.05	0.51 ± 0.08	0.95 ± 0.02	0.30 ± 0.05
9	0.95 ± 0.03	0.30 ± 0.10	0.89 ± 0.07	0.41 ± 0.15	0.92 ± 0.04	-0.37 ± 0.12
10	0.94 ± 0.04	-0.30 ± 0.14	0.89 ± 0.07	-0.41 ± 0.15	0.92 ± 0.04	0.37 ± 0.12
11	0.95 ± 0.03	0.30 ± 0.10	0.88 ± 0.07	-0.46 ± 0.13	0.96 ± 0.04	0.25 ± 0.15
12	0.94 ± 0.04	-0.30 ± 0.15	0.88 ± 0.06	0.46 ± 0.13	0.96 ± 0.04	-0.24 ± 0.16

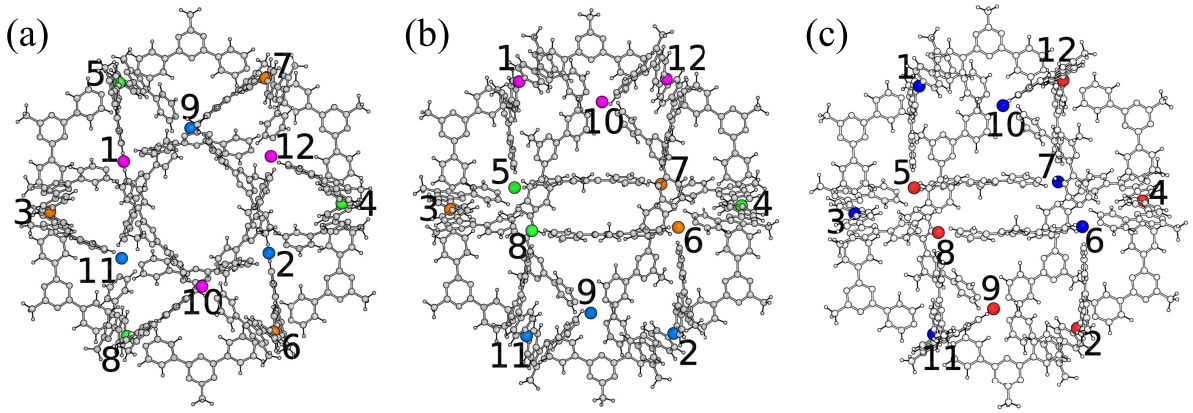

Fig. 6 The relationships between optimized geometries and local coordination structures; (a) the top view and (b) the side view of S_6 optimized structure in the gas phase and (c) the side view of C_i optimized structure in the solution phase.

Table 8 Weights (%) of dominant Slater determinants in electronic ground state of each Pd^{2+} ion in $[Pd_{12}L_{24}]^{24+}$. Values larger than 1.0 % are shown for clarity

gas	M	1	2	3	4	5	6	7	8	9	10	11	12
	$(C_1^{(0)})^2$	89.7	89.7	89.2	89.2	89.0	89.1	89.0	88.9	89.5	89.5	89.6	89.6
	$(C_2^{(0)})^2$	2.9	2.9	3.4	3.4	3.4	3.4	3.5	3.5	3.0	3.0	3.0	3.0
	$(C_3^{(0)})^2$	2.9	2.9	3.4	3.4	3.4	3.4	3.5	3.5	3.0	3.0	3.0	3.0
	$(C_4^{(0)})^2$	1.1	1.1	1.0	1.0	1.0	1.0	1.0	1.0	1.1	1.1	1.1	1.1
	sum	96.6	96.6	97.0	96.9	96.9	97.0	96.9	96.8	96.5	96.5	96.6	96.6
solution	M	1	2	3	4	5	6	7	8	9	10	11	12
	$(C_1^{(0)})^2$	96.1	96.1	95.5	95.4	94.7	94.7	93.9	93.9	95.6	95.6	95.3	95.3
	$(C_2^{(0)})^2$							1.2	1.2				
	$(C_3^{(0)})^2$							1.2	1.2				
	$(C_4^{(0)})^2$	2.2	2.2	2.0	2.0	1.9	1.9	1.8	1.8	2.1	2.1	2.1	2.1
	sum	98.3	98.3	97.5	97.4	96.6	96.6	98.1	98.1	97.8	97.7	97.4	97.4
solution with BF_4^-	M	1	2	3	4	5	6	7	8	9	10	11	12
	$(C_1^{(0)})^2$	90.8	90.7	91.5	91.4	86.2	86.2	91.5	91.5	91.9	92.0	90.8	90.8
	$(C_2^{(0)})^2$	3.1	3.1	2.7	2.7	5.4	5.3	2.7	2.7	2.4	2.3	3.1	3.1
	$(C_3^{(0)})^2$	3.1	3.1	2.7	2.7	5.4	5.3	2.7	2.7	2.4	2.3	3.1	3.1
	$(C_4^{(0)})^2$	1.4	1.4	1.5	1.5			1.5	1.5	1.7	1.7	1.4	1.4
	$(C_5^{(0)})^2$					1.0	1.0						
	sum	98.4	98.4	98.3	98.4	97.9	97.9	98.3	98.4	98.3	98.3	98.5	98.4

direction for future work.

Conflicts of interest

There are no conflicts to declare.

Acknowledgements

We thank Dr. Sota Sato for his valuable advice. YY also thanks the Grant-in Aid for JSPS Fellows. This work was financially supported by JSPS KAKENHI Grant Number JP17H03009 and JP18J14387. Theoretical computations were largely performed using Research Center for Computational Science, Okazaki, Japan.

Notes and references

1 Q.-F. Sun, J. Iwasa, D. Ogawa, Y. Ishido, S. Sato, T. Ozeki, Y. Sei, K. Yamaguchi and M. Fujita, *Science*, 2010, **328**, 1144–1147.

2 J. Bunzen, J. Iwasa, P. Bonakdarzadeh, E. Numata, K. Rissanen, S. Sato and M. Fujita, *Angew. Chem.*, 2012, **124**, 3215–3217.

3 D. Fujita, Y. Ueda, S. Sato, H. Yokoyama, N. Mizuno, T. Kumasaka and M. Fujita, *Chem*, 2016, **1**, 91–101.

4 D. Fujita, Y. Ueda, S. Sato, N. Mizuno, T. Kumasaka and M. Fujita, *Nature*, 2016, **540**, 563–566.

5 D. Fujita, H. Yokoyama, Y. Ueda, S. Sato and M. Fujita, *Angew. Chem. Int. Ed.*, 2015, **54**, 155–158.

6 R. Chakrabarty, P. S. Mukherjee and P. J. Stang, *Chem. Rev.*, 2011, **111**, 6810–6918.

7 T. R. Cook and P. J. Stang, *Chem. Rev.*, 2015, **115**, 7001–7045.

8 P. J. Stang and B. Olenyuk, *Acc. Chem. Res.*, 1997, **30**, 502–518.

9 J. S. Mugridge, R. G. Bergman and K. N. Raymond, *Angew. Chem. Int. Ed.*, 2010, **49**, 3635–3637.

10 D. Fiedler, R. G. Bergman and K. N. Raymond, *Angew. Chem. Int. Ed.*, 2004, **43**, 6748–6751.

11 D. M. Kaphan, M. D. Levin, R. G. Bergman, K. N. Raymond and F. D. Toste, *Science*, 2015, **350**, 1235–1238.

12 P. S. Nerenberg and T. Head-Gordon, *Curr. Opin. Struct. Biol.*, 2018, **49**, 129–138.

13 Z. Jing, C. Liu, S. Y. Cheng, R. Qi, B. D. Walker, J.-P. Piquemal and P. Ren, *Annu. Rev. Biophys.*, 2019, **48**, 371–394.

14 D. Bedrov, J.-P. Piquemal, O. Borodin, A. D. MacKerell, Jr., B. Roux and C. Schröder, *Chem. Rev.*, 2019, **119**, 7940–7995.

15 M. Gaus, H. Jin, D. Darren, A. S. Christensen, P. Goyal, M. Elstner and Q. Cui, *J. Chem. Theory Comput.*, 2015, **11**, 4205–4219.

16 M. Vujović, M. Huynh, S. Steiner, P. Garcia-Fernandez, M. Elstner, Q. Cui and M. Gruden, *J. Comput. Chem.*, 2019, **40**, 400–413.

17 S. Iuchi, A. Morita and S. Kato, *J. Chem. Phys.*, 2004, **121**, 8446.

18 S. Iuchi, *J. Chem. Phys.*, 2012, **136**, 064519.

19 J. S. Griffith, *The theory of transition-metal ions*, Cambridge University Press, New York, 1961.

20 S. Iuchi and N. Koga, *J. Chem. Phys.*, 2014, **140**, 024309.

21 Y. Matsumura, S. Iuchi and H. Sato, *Phys. Chem. Chem. Phys.*, 2018, **20**, 1164–1172.

22 N. Shibata, H. Sato, S. Sakaki and Y. Sugita, *J. Phys. Chem. B*, 2011, **115**, 10553–10559.

23 D. Bashford and D. A. Case, *Annu. Rev. Phys. Chem.*, 2000, **51**, 129–152.

24 G. D. Hawkins, C. J. Cramer and D. G. Truhlar, *Chem. Phys. Lett.*, 1995, **246**, 122–129.

25 G. D. Hawkins, C. J. Cramer and D. G. Truhlar, *J. Phys. Chem.*, 1996, **100**, 19824–19839.

26 W. C. Still, A. Tempczyk, R. C. Hawley and T. Hendrickson, *J. Am. Chem. Soc.*, 1990, **112**, 6127–6129.

27 H. Nguyen, A. Pérez, B. Sherry and C. Simmerling, *J. Chem. Theory Comput.*, 2015, **11**, 3714–3728.

28 A. V. Onufriev and D. A. Case, *Annu. Rev. Biophys.*, 2019, **48**, 275–296.

29 P. W. J. M. Frederix, I. Patmanidis and S. J. Marrink, *Chem. Soc. Rev.*, 2018, **47**, 3470–3489.

30 F. Giberti, M. Salvalaglio, M. Mazzotti and M. Parrinello, *Cryst. Growth Des.*, 2017, **17**, 4137–4143.

31 H. H. Arefi and T. Yamamoto, *J. Chem. Phys.*, 2017, **147**, 211102.

32 T. Yamamoto, H. Arefi, S. Shanker, H. Sato and S. Hiraoka, *J. Phys. Chem. Lett.*, 2018, **9**, 6082–6088.

33 J.-F. Truchon, B. M. Pettitt and P. Labute, *J. Chem. Theory Comput.*, 2014, **10**, 934–941.

34 D. S. Palmer, A. I. Frolov, E. L. Ratkova and M. V. Fedrov, *J. Phys.: Condens. Matter*, 2010, **22**, 492101.

35 V. Sergiievskyi, G. Jeanmairet, M. Levesque and D. Borgis, *J. Chem. Phys.*, 2015, **143**, 184116.

36 T. Fujita and T. Yamamoto, *J. Chem. Phys.*, 2017, **147**, 014110.

37 M. Mammen, E. I. Shakhnovich, J. M. Deutch and G. M. Whitesides, *J. Org. Chem.*, 1998, **63**, 3821–3830.

38 P. Y. Ayala and H. B. Schlegel, *J. Chem. Phys.*, 1998, **108**, 2314–2325.

39 S. Grimme, *Chem. Eur. J.*, 2012, **18**, 9955–9964.

40 W. J. Pietro, E. S. Blurock, R. F. H. Jr., W. J. Hehre, D. J. Defrees and R. F. Stewart, *Inorg. Chem.*, 1981, **20**, 3650–3654.

41 W. J. Hehre, R. F. Stewart and J. A. Pople, *J. Chem. Phys.*, 1969, **51**, 2657–2664.

42 M. B. Darkhovskii and A. L. Tchougreeff, *J. Phys. Chem. A*, 2004, **108**, 6351–6364.

43 J. Wang, R. M. Wolf, J. W. Caldwell, P. A. Kollman and D. A. Case, *J. Comput. Chem.*, 2004, **25**, 1157–1174.

44 V. Barone and M. Cossi, *J. Phys. Chem. A*, 1998, **102**, 1995–2001.

45 M. Cossi, N. Rega, G. Scalmani and V. Barone, *J. Comput. Chem.*, 2003, **24**, 669–681.

46 C. I. Bayly, P. Cieplak, W. D. Cornell and P. A. Kollman, *J. Phys. Chem.*, 1993, **97**, 10269–10280.

47 D. Andrae, U. Häußermann, M. Dolg, H. Stoll and H. Preuß, *Theor. Chim. Acta*, 1990, **77**, 123–141.

48 R. Krishnan, J. S. Binkley, R. Seeger and J. A. Pople, *J. Chem. Phys.*, 1980, **72**, 650–654.

49 U. C. Singh and P. A. Kollman, *J. Comput. Chem.*, 1984, **5**, 129–145.

50 B. H. Besler, K. M. Merz Jr. and P. A. Kollman, *J. Comput. Chem.*, 1990, **11**, 431–439.

51 D. Case, R. Betz, D. Cerutti, T. C. III, T. Darden, R. Duke, T. Giese, H. Gohlke, A. Goetz, N. Homeyer, S. Izadi, P. Janowski, J. Kaus, A. Kovalenko, T. Lee, S. LeGrand, P. Li, C. Lin, T. Luchko, R. Luo, B. Madej, D. Mermelstein, K. Merz, G. Monard, H. Nguyen, H. Nguyen, I. Omelyan, A. Onufriev, D. Roe, A. Roitberg, C. Sagui, C. Simmerling, W. Botello-Smith, J. Swails, , R. Walker, J. Wang, R. Wolf, X. Wu, L. Xiao and P. Kollman, *AMBER 2016*, 2016, University of California, San Francisco.

52 D. L. Carroll's FORTRAN genetic algorithm driver.

53 D. Liu and J. Nocedal, *Mathematical Programming B*, 1989, **45**, 503–528.

54 J. Nocedal, *Mathematics of computation*, 1980, **35**, 773–782.

55 D. J. Wales, `OPTIM`*: A program for geometry optimisation and pathway calculations*, http://www-wales.ch.cam.ac.uk/software.html.

56 A. Bondi, *J. Phys. Chem.*, 1964, **68**, 441–451.

57 M. Mantina, A. C. Chamberlin, R. Valero, C. J. Cramer and D. G. Truhlar, *J. Phys. Chem. A*, 2009, **113**, 5806–5812.

58 Y. Zhao and D. G. Truhlar, *J. Chem. Phys.*, 2006, **125**, 194101.

59 P. J. Hay and W. R. Wadt, *J. Chem. Phys.*, 1985, **82**, 299–310.

60 W. J. Hehre, R. Ditchfield and J. A. Pople, *J. Chem. Phys.*, 1972, **56**, 2257–2261.

61 P. C. Hariharan and J. A. Pople, *Theor. Chim. Acta*, 1973, **28**, 213–222.

62 M. W. Schmidt, K. K. Baldridge, J. A. Boatz, S. T. Elbert, M. S. Gordon, J. H. Jensen, S. Koseki, N. Matsunaga, K. A. Nguyen, S. Su, T. L. Windus, M. Dupuis and J. A. Montgomery, *J. Comput. Chem.*, 1993, **14**, 1347–1363.

63 Y. Zhao and D. G. Truhlar, *Theor. Chem. Acc.*, 2008, **120**, 215–241.

64 Y. Zhao and D. G. Truhlar, *Acc. Chem. Res.*, 2008, **41**, 157–167.

65 T. L. Hill, *An introduction to statistical thermodynamics*, Dover Publications, New York, 1986.

66 Z. Liu, S. Huang and W. Wang, *J. Phys. Chem. B*, 2004, **108**, 12978–12989.

67 N. L. Allinger, X. Zhou and J. Bergsma, *J. Mol. Struct. (THEOCHEM)*, 1994, **312**, 69–83.

68 C. Mavroyannis and M. J. Stephen, *Molec. Phys.*, 1962, **5**, 629–638.

69 A. Stone, *The theory of intermolecular forces*, Oxford University Press, New York, 2nd edn., 2013.

70 H. Sato and F. Hirata, *J. Phys. Chem. A*, 2002, **106**, 2300–2304.

71 S. Sakamoto, M. Fujita, K. Kim and K. Yamaguchi, *Tetrahedron*, 2000, **56**, 955–964.

72 K. Yamaguchi, *J. Mass Spectrom.*, 2003, **38**, 473–490.

73 T. Pilati and A. Forti, *J. Appl. Cryst.*, 1998, **31**, 503–504.

74 M. Weller, T. Overton, J. Rourke and F. Armstrong, *Inorganic Chemistry*, Oxford University Press, Oxford, 7th edn., 2014.